Pressure-driven DNA transport across an artificial nanotopography

2009 New J. Phys. 11 075032

(http://iopscience.iop.org/1367-2630/11/7/075032)

New Journal of Physics
The open-access journal for physics

Pressure-driven DNA transport across an artificial nanotopography

J T Del Bonis-O'Donnell, W Reisner and D Stein[1]
Department of Physics, Brown University, Providence, RI 02912, USA
E-mail: derek_stein@brown.edu

New Journal of Physics **11** (2009) 075032 (24pp)
Received 22 January 2009
Published 31 July 2009
Online at http://www.njp.org/
doi:10.1088/1367-2630/11/7/075032

Abstract. The pressure-driven transport of DNA was studied in slit-like nanochannels with an embedded nanotopography consisting of linear arrays of nanopits. We imaged individual DNA molecules moving single-file down the nanopit array, undergoing sequential pit-to-pit hops using fluorescence video microscopy. Distinct transport dynamics were observed depending on whether a molecule could occupy a single pit, or was forced to subtend multiple pits. We interpret these results in terms of a scaling theory of the free energy of polymer chains in a linear array of pits. Molecules contained within a single pit are predicted to face an entropic free energy barrier, and to hop between pits by thermally activated transport. Molecules that subtend multiple pits, on the other hand, can transfer DNA contour from upstream to downstream pits in response to an applied fluid flow, which lowers the energy barrier. When the trailing pit completely empties, or when the leading pit reaches its capacity, the energy barrier is predicted to vanish, and the low-pressure, thermally activated transport regime gives way to a high-pressure, dissipative transport regime. These results contribute to our understanding of polymers in nanoconfined environments, and may guide the development of nanoscale lab-on-a-chip applications.

[1] Author to whom any correspondence should be addressed.

Contents

1. Introduction

Over the past decade, nanotechnology has inspired a number of single-molecule approaches to the separation, manipulation and analysis of DNA. These methods include artificial gels, microfluidic and nanofluidic channels and solid state nanopores [1]–[13]. Nanofluidic devices offer control over individual DNA molecules by exploiting properties of polymers that are unique to the nanoscale. For instance, when a DNA molecule is confined in a channel whose critical dimensions fall below the average radius of gyration, R_g, self-exclusion interactions between the segments strongly influence molecular conformation, resulting in the spontaneous stretching of DNA. A genome can consequently be stretched out in 100×100 nm nanochannels, enabling its optical analysis [9]–[13]. Furthermore, by restricting the internal degrees of freedom of a polymer, nanoscale confinement gives rise to entropic forces that play a central role in devices such as entropic trap arrays [8]. Recently, Reisner *et al* [13] reported a new way to manipulate DNA configurations that relies on both entropy and excluded volume effects. A square lattice of nanoscale depressions (nanopits) embedded in slit-like nanochannels was shown to localize molecules on a chip, and create complex conformations that straddle multiple depressions [14]. These previous studies were restricted to equilibrium behavior. Here, we consider the driven transport of DNA confined in nanopit arrays. We report measurements and theoretical analysis of pressure-driven DNA dynamics that reveal how the nanotopography of a fluidic device dictates the free energy landscape for DNA, which in turn governs its transport.

The geometry of the nanofluidic devices we studied, shown in figures 1(a) and (b), consisted of slit-like nanochannels with a height $h \approx 100$ nm below the characteristic size of λ-phage DNA in solution ($R_g = 0.73\,\mu$m [15]). The topography of the slit included $H \approx 100$ nm-deep square nanopits, either 500×500 nm or $1 \times 1\,\mu$m in size. The nanopits were

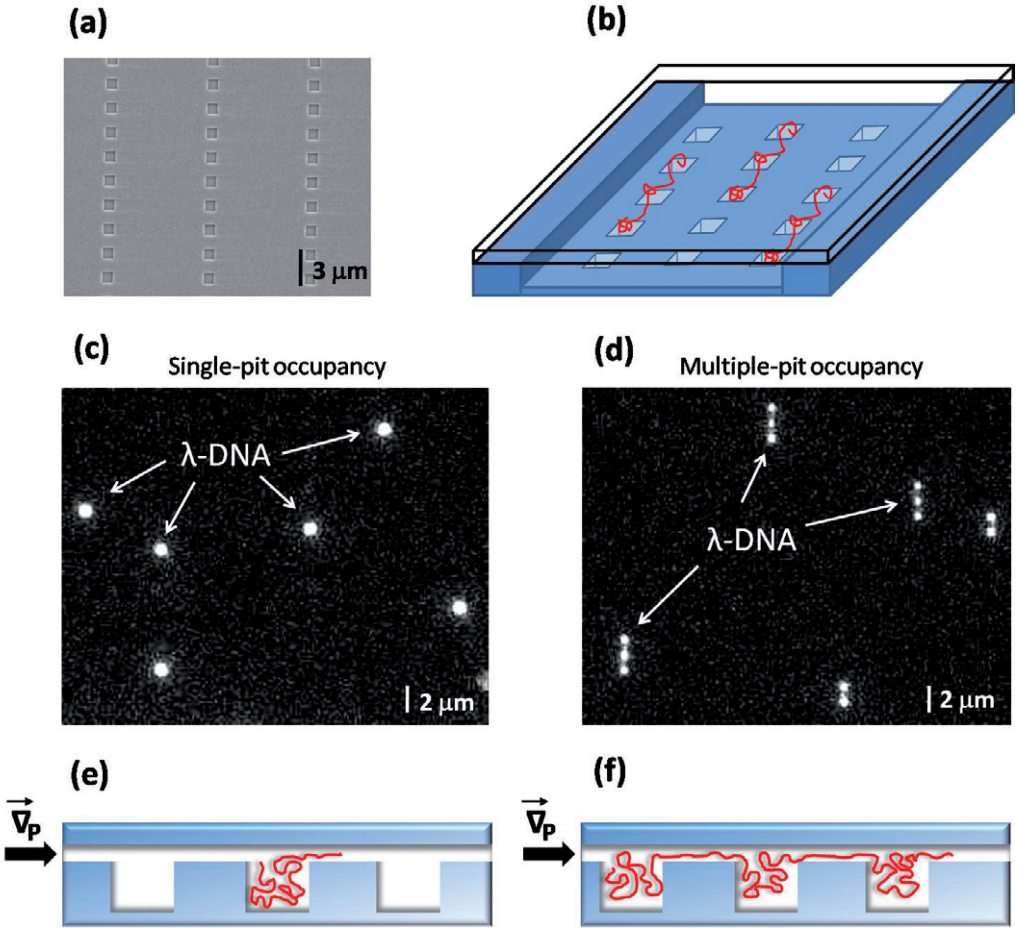

Figure 1. (a) Scanning electron micrograph of typical $1 \times 1\,\mu$m square pits embedded in a nanoslit at 1 μm intervals. This particular device was not used for this study. (b) Illustration of DNA conformations in an enclosed nanopit array device. Molecules align themselves with the linear pit array by occupying a number of successive pits. (c) and (d) Epifluorescent images of stained λ-phage DNA molecules confined in (c) a 107 ± 1 nm deep slit embedded with $1 \times 1\,\mu$m pits spaced 2 μm apart, and (d) a 90 ± 2 nm deep slit embedded with 500×500 nm pits spaced 1 μm apart. The thin slit region of the device is oriented parallel to the plane of the images. (e) and (f) Schematic side views of DNA molecules driven along linear arrays of nanopits by an applied pressure gradient, ∇p. Two situations are shown: (e) single-pit occupation and (f) multiple-pit occupation.

arranged in periodic linear arrays with micrometer-scale spacing, d. When λ-DNA was confined in this particular nanotopography, the molecules tended to occupy one or multiple pits, depending on their size, as shown in figures 1(c) and (d).

The partitioning of a molecule, i.e. how it distributes its contour between pits and the slit, can be understood by considering the differences in free energy of the molecule in each region [14]. In the slit, the high degree of confinement imposes a high free energy cost on

a molecule, whereas in the increased volume of a pit, a molecule can increase its entropy and thereby lower its free energy. A molecule cannot insert an unlimited amount of contour in a single pit, however, because excluded volume interactions raise the free energy cost of occupying that pit. The result is that DNA molecules can either be entirely contained within a single pit, or be forced to subtend multiple pits, as shown schematically in figures 1(e) and (f), respectively. The two regimes were predicted to depend upon the length of the molecule and the size and geometry of the pits in a manner that was consistent with experiment. The multiple-pit conformations were subject to thermal fluctuations, which could vary the number of occupied pits.

In the present study, a constant pressure applied across the nanofluidic device caused DNA molecules to travel down the linear nanopit arrays in single file by pit-to-pit hops. The pits restricted the motion of DNA in the fluid flow in a manner that was reminiscent of electrophoretic DNA transport in entropic trap arrays [8] (see movie 1, available at stacks.iop.org/NJP/11/075032/mmedia). In contrast with entropic traps, however, we explore DNA transport in nanopit structures whose height and lateral dimensions were all submicrometer in scale, resulting in molecular conformations that could simultaneously occupy multiple pits (see movie 2). Indeed, we found that when the pits were large enough to contain the entire DNA contour length, pressure-driven DNA transport across nanopit arrays corresponded closely to the model developed by Han *et al* [16], with a free energy barrier giving rise to a statistical, thermally activated hopping mechanism. However, the model failed to predict the transport behavior when a molecule occupied multiple pits. Here we develop a theoretical model that explains all the observed features of DNA transport. The model is based on the free energy landscape for a polymer in the nanopit array geometry, subject to the viscous drag of a pressure-driven fluid flow.

2. Materials and methods

2.1. Nanofluidic device fabrication

The nanopit devices were fabricated on fused silica wafers (HOYA) by first using electron beam lithography to define nanopits on one surface, then UV contact photolithography to define a nanoslit on the same surface, and finally direct bonding to a second, coverslip-thick fused-silica chip to seal the channels. Fused silica wafers were chosen due to their transparency, their well-defined surface chemistry, and the ease with which they can be bonded. The nanopits were patterned by electron beam lithography (JEOL) in zep520A resist [17], which was then developed in ZED-N50 (Zeon corporation). We have found that zep520A resist is superior to PMMA for this process because zep520A combines high resolution with excellent plasma resistance. These attractive properties obviate the need for thick PMMA bilayers or for angled evaporation of metals after ebeam exposure that would otherwise be needed to increase resistance to the plasma etch. A $CF_4 : CHF_3$ reactive ion etching (RIE) process was used to transfer the pattern to the underlying silica. The zep520A resist was removed by 5–10 min of heated sonnication in Remover 1165 (Shipley). Contact UV lithography in 1.5 μm-thick AZ5214 photoresist (Clariant) then exposed a 450 μm-long, 50 μm-wide nanoslit over the nanopit array, which was then etched to a depth of 100 nm (see figure 1(a)). U-shaped microchannels were incorporated by a final UV contact lithography and etching step to facilitate the transfer of buffer into the nanofluidic devices. The 50 μm-wide, 1 μm-deep microchannels were located on either side of the nanoslit, leading to circular reservoirs. Access holes were

sandblasted through the substrate at the reservoirs, and the chip was sealed using direct quartz–quartz bonding to 150 μm-thick fused silica coverglass (Valley Design), permitting the use of high numerical aperture oil immersion microscope objectives. The nanoslit, nanopit and microchannel etch depths were measured using a profilometer. The direct bonding process was performed after first cleaning the chips for 20 min in piranha solution (sulfuric acid/hydrogen peroxide 2 : 1), 20 min in RCA1 (deionized water/hydrochloric acid/hydrogen peroxide 5 : 1 : 1) and 20 min in RCA2 (deionized water/ammonium hydroxide/hydrogen peroxide 5 : 1 : 1). The RCA1 and RCA2 solutions were heated to 80 °C.

2.2. DNA preparation

λ-phage DNA molecules (48.5 kbps, $L = 16.5\,\mu$m, New England Biolabs) were used in all experiments. Stock DNA solution (457 μg ml^{-1}) was heated at 65 °C for 10 min and then quenched in an ice bath. The DNA was diluted to a concentration of 10 μg ml^{-1} and stained with YOYO-1 dye in degassed 50 mM Tris-HCl buffer at a ratio of 1 dye molecule per 10 base pairs. We estimate that this staining ratio increases the contour length of the molecule to approximately 18.6 μm [13]. DNA suspensions used in experiments were further diluted to 0.5–1 μg ml^{-1} in 50 mM Tris-HCl. Beta-mercaptoethanol was added at 2% by volume to reduce photobleaching and photocleavage of the DNA after exposure to the light source [18]. We have found that low ionic strength buffers (<10 mM) tend to increase DNA fragmentation while high ionic strength buffers (>100 mM) tend to reduce fluorescence. We chose the 50 mM Tris-HCl buffer as a best compromise between these limits. The nanofluidic device was loaded with DNA by pipetting solution into the reservoirs before mounting the chip onto a custom-made sample holder. O-rings sealed the chip to the holder, while luer connections and tubing connected the sample holder to the pressure control system (see figure 2).

2.3. Acquisition of video data for DNA transport in nanopit arrays

Single DNA molecules were imaged in the nanopit arrays using a videomicroscopy setup consisting of an inverted microscope (Nikon Eclipse TE2000-U) with a 100×, 1.4 N.A. oil immersion objective (Nikon) and an EMCCD camera (Andor iXon). Fluorescence illumination was supplied, and its intensity controlled, by a 120 W metal-halide lamp (XEFO Xcite 120) with an attached shutter (Uniblitz Model VCM-D1). We chose to reduce the maximum lamp intensity by 25% as a good compromise between obtaining a strong fluorescence signal and minimizing photocleavage and photobleaching of the molecules. To further minimize UV-induced damage, the shutter only opened during the exposure time of the camera.

A constant external pressure drop, generated by an air pump, drove fluid and DNA molecules through the microchannels and the nanoslit. The fluid flow was directed parallel to the linear arrays of pits in the nanoslit. The pressure applied to each reservoir could be switched on or off, and varied using a series of leak valves, illustrated in figure 2. Before introducing DNA into the nanoslit, high pressures were applied across the microchannels to clear out air bubbles that might have been introduced during the wetting of the chip.

DNA molecules were then driven into the nanoslit. Static conformations of the molecules in the pit arrays, recorded with the pressure switched off, are shown in figures 1(c) and (d). Videos of pressure-driven DNA transport in the arrays were then recorded as the pressure drop across the nanoslit was increased from 1 to 40 mbar in increments of $\pm$1 mbar at lower pressures and

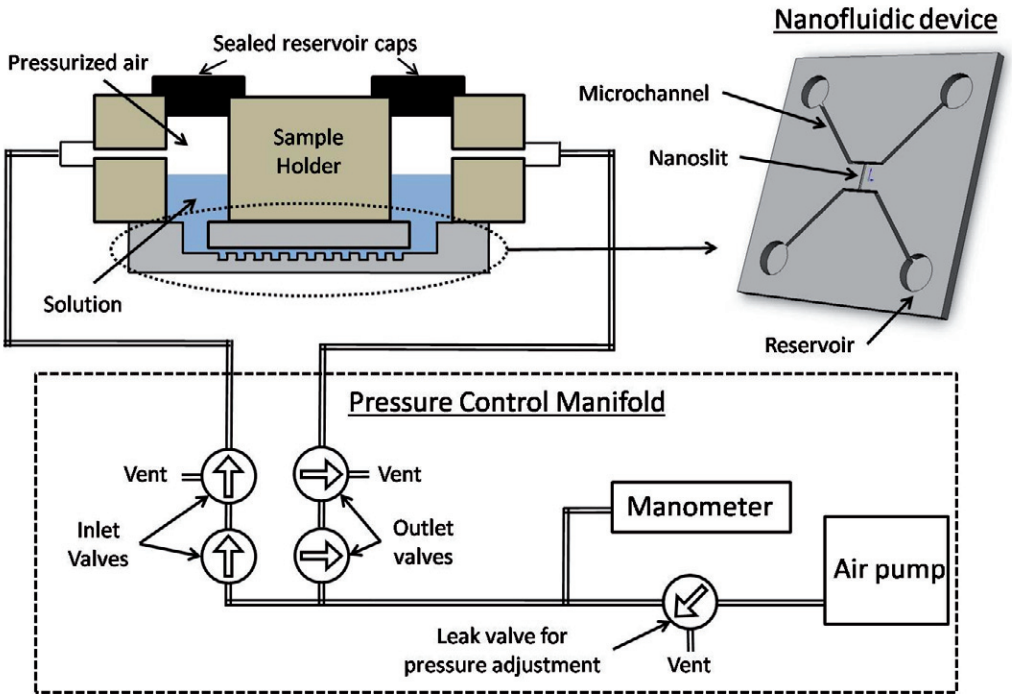

Figure 2. Schematic of the experiment. Top right: a nanoslit containing an embedded nanopit array was located at the center of the nanofluidic device. The nanoslit was flanked by two deep microchannels through which fluid could be easily flushed. Reservoirs located at the four corners of the device provided access to the ends of each microchannel. Top left: the nanofluidic device was mounted to a sample holder that held the device above the microscope, and allowed fluid to be driven across the nanoslit by a pressure control manifold (below). The pressure supplied by the air pump was regulated using an adjustable leak valve. Pressure was applied across the channel by closing the outlet valves, while opening the inlet valve and closing the inlet vent.

5±1 mbar at higher pressures. In addition, videos of DNA transport were recorded in regions of the device where the nanoslit contained no nanopits, using the same devices and for the same pressure range. The velocity of unimpeded DNA transport in the slit, v_{slit}, was used to calibrate the true fluid velocity in the slit, v, at a given pressure drop. This method of establishing changes in v is superior to measuring the pressure drop across the device because we expect $v_{\text{slit}} \propto v$, whereas inferring v from a manometer reading is sensitive to variations in the fluidic impedance of the inlet, the outlet and the tubing. All videos of DNA transport ranged in size from 120 frames at low pressures to 200 frames at high pressures. The frame rates were 0.2002 Hz (low pressures) and 9.829 Hz (high pressures), respectively. The exposure time for each image was 0.1 s. Each video included 3–10 molecules.

2.4. Image analysis

The DNA transport videos were analyzed using a custom-developed Matlab program. Each frame was analyzed by first subtracting the background, and then applying Gaussian filters

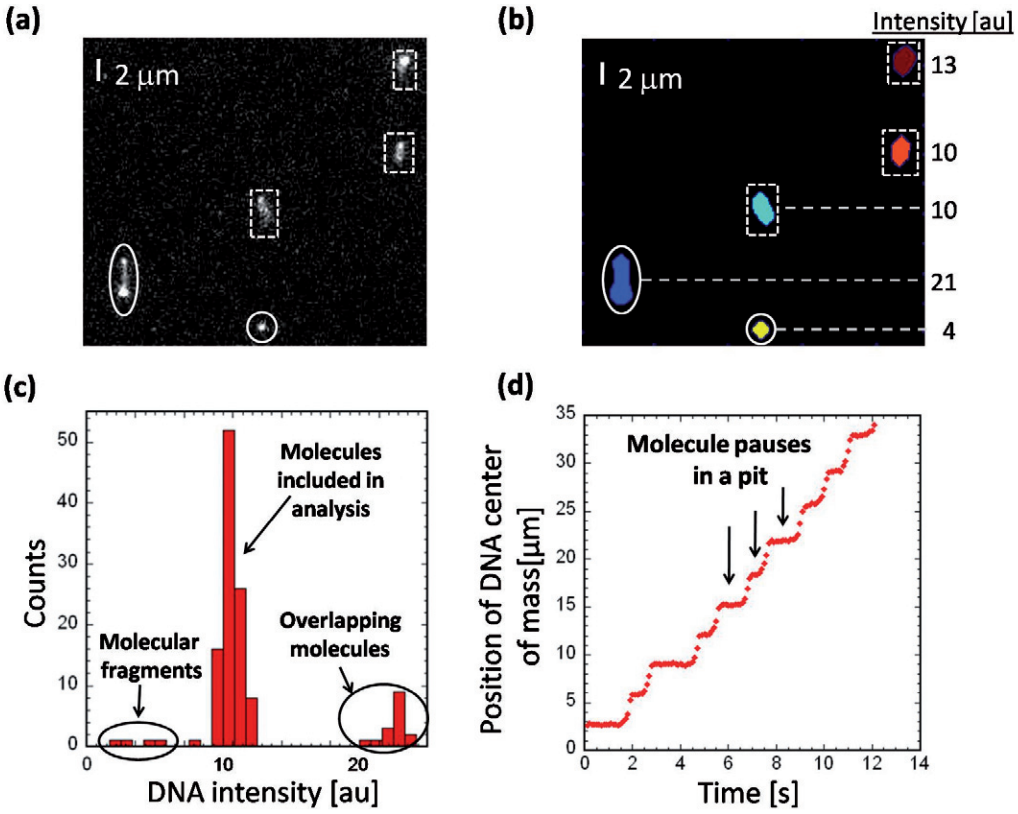

Figure 3. Image acquisition and analysis. (a) A typical image of fluorescent λ-DNA molecules being driven across a nanopit array by an applied pressure of 40 mbar. The slit was 107 ± 1 nm deep and contained linear arrays of $1 \times 1\ \mu$m pits spaced $2\ \mu$m apart. Boxes indicate molecules that were included in the transport analysis. The circles indicate overlapping or fragmented molecules that were rejected by the analysis. (b) The same image after analysis. The integrated fluorescence intensity of each identified molecule is indicated (in arbitrary units). (c) An intensity histogram for a 200-frame video containing five computer-identified molecules. A filter removed the fragmented and overlapping molecules (circled) from the analysis. (d) The center-of-mass position of a typical λ-DNA molecule is plotted as a function of time for transport across the same nanopit array at an applied pressure of 22 mbar. The plateaus, of which a few are indicated, corresponded to the locations of pits, where the DNA became entirely confined for varying times.

and dilation transformations from the image processing toolbox library to isolate and identify the molecules. The center of mass of each molecule in the image was then calculated from the relative intensity data. An example of the analysis protocol for a sample image is shown in figure 3(b). Single, unbroken λ-DNA molecules were distinguished from fragments and overlapping molecules in the acquired images by analyzing histograms of the intensity data (see figure 3). A filtering process removed the outlying peaks from the analysis, as these data were judged to correspond to either fragmented or entangled DNA molecules.

In order to follow the progress of the molecules through a video, it was necessary to identify and match molecules in consecutive frames. For each molecule in a given frame, displacement vectors were calculated to each molecule in the previous frame. The pairs of molecules giving the smallest displacements were identified as being the same molecules in both frames. The velocity of the center of mass of each molecule in a frame was then calculated using the frame rate and the calculated displacement from the previous frame (see figure 3(d)). We obtained an average DNA velocity by taking the mean velocity of each molecule in every frame.

3. Results

Pressure-driven DNA transport was studied in three different nanopit array device geometries: (i) $1 \times 1\,\mu$m pits spaced $2\,\mu$m apart ($h = H = 107 \pm 1$ nm), (ii) 500×500 nm pits spaced $2\,\mu$m apart ($h = H = 107 \pm 1$ nm) and (iii) 500×500 nm pits spaced $1\,\mu$m apart ($h = 90 \pm 2$ nm, $H = 102 \pm 1$ nm). The pit dimensions determined whether single-pit or multiple-pit DNA configurations occurred at equilibrium. The λ-DNA molecules fit completely within a single pit in the $1 \times 1\,\mu$m pit device, spanned 2 pits in the device with 500×500 nm pits and $2\,\mu$m spacings and spanned 2–3 pits in the device with 500×500 nm pits and $1\,\mu$m spacings.

Figure 4 shows examples of DNA molecules traversing two different nanopit arrays. In both cases, the molecules moved along the linear array by making sequential pit-to-pit hops. The motion was strictly single file, as molecules were not observed to stray laterally. The pressure-driven flow did not alter the single-pit or multiple-pit character of the DNA configurations. In the array of large pits, the DNA would fall completely into a single pit before any contour extended toward the next pit (figure 4(a)). In the array of smaller pits, at least two pits were occupied at all times (figure 4(b)). Furthermore, the fluorescence intensity increased in the leading pit, and decreased in the trailing pits between steps, indicating a transfer of DNA contour from upstream to downstream pits.

The velocity of λ-DNA molecules traversing the nanopit arrays, v_{pits}, was measured together with the DNA velocity in the slit, v_{slit}, for all the device geometries and applied pressures tested. The plot of v_{nanopit} versus v_{slit}, shown in figure 5, reveals a clear difference between DNA transport in the single-pit occupancy, $1 \times 1\,\mu$m pit devices, and in the multiple-pit occupancy, 500×500 nm pit devices. The former geometry gave rise to nonlinear behavior over the entire range of v_{slit}, and was well described by an exponential function similar to one derived by Han *et al* [16] $v_{\text{pits}} = v_0 \exp(k v_{\text{slit}}^{-1})$. The 500×500 nm pits, by contrast, exhibited linear transport behavior over the entire range of v_{slit} when the spacing between pits was $2\,\mu$m. In the case where the spacing between pits was $1\,\mu$m, linear behavior was only observed for elevated v_{slit}, while v_{pits} was both nonlinear and highly suppressed at low v_{slit}. The transition from linear to nonlinear transport behavior occurred at a v_{slit} of approximately $4\,\mu\text{m s}^{-1}$.

Figure 6 hints at what physics may lie behind these observations. The time evolution of a single DNA molecule traveling along a line of 500×500 nm pits spaced $1\,\mu$m apart is presented for both high and low pressures. The molecule occupied each pit for the same amount of time at the high pressure, whereas there was a clear variance in the residence times at the low pressure. Histograms of the residence times of molecules in each pit reveal a normal distribution of dwell times under a high applied pressure ($v_{\text{slit}} = 11.2\,\mu\text{m s}^{-1}$), and dwell times that were exponentially distributed in the long dwell time limit under a low applied pressure ($v_{\text{slit}} = 1.21\,\mu\text{m s}^{-1}$). This variance suggests that transport was stochastic at low pressures. Similar stochastic transport behavior was also observed in the $1 \times 1\ \mu$m nanopit devices, where

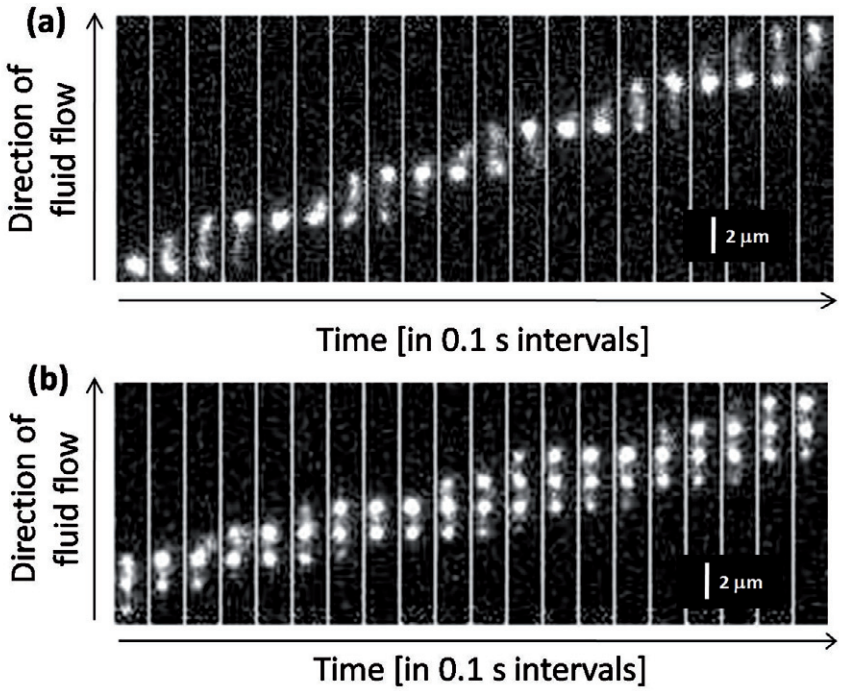

Figure 4. Fluorescent images of λ-DNA traveling across a nanopit array under an applied pressure of 40 mbar. (a) An entire molecule was able to occupy a single 1×1 μm pit and then squeeze through the 107 ± 1 nm-high, 2 μm-long slit region to the next pit. (b) A migrating molecule was forced to occupy multiple 500×500 nm pits, spaced 1 μm apart in a 90 ± 2 nm-high slit. The fluorescence intensity corresponded to the amount of DNA contour in a given pit.

the exponential dependence of v_{pits} on v_{slit}^{-1} was observed (figure 5). These observations lead us to hypothesize that the transport mechanism for DNA is thermally activated for pits that are large enough to trap an entire molecule, or for the case of multiple-pit occupancy at sufficiently low pressure. The transport of molecules in multiple-pit states under high pressures appears to proceed by a deterministic pit-to-pit process. These notions have motivated our theoretical investigation of the energy landscape for DNA transport below.

4. Theoretical model of DNA transport across nanopit arrays

Our observations of DNA transport across linear nanopit arrays can be understood in terms of a simple model of the free energy landscape, and how this is affected by the application of a pressure-driven fluid flow. Reisner *et al* modeled the static situation of DNA partitioning its contour length between N pits and the $N-1$ 'linkers' that must span the slit region between the pits. They calculated the reduction in free energy that occurs when a section of DNA in the highly confined, and hence entropically unfavorable, slit region inserts into a pit. By minimizing the total free energy for a molecule of length L, the equilibrium partitioning of DNA between the pits and the slit could be determined for a given N. Furthermore, the probability of a molecule occupying N pits could be obtained from the equilibrium free energies at each occupancy value N using the appropriate Boltzmann weighting factor. Here, we present a model of DNA

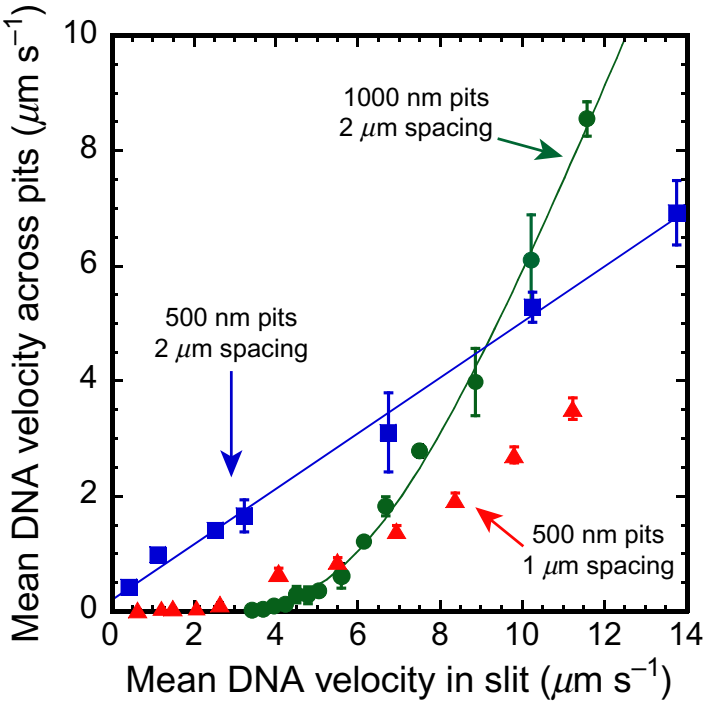

Figure 5. Pressure-driven DNA transport across nanopit arrays. (v_{pits}) is plotted against (v_{slit}). Data were collected for three devices with varying dimensions: ●: $h = 107 \pm 1$ nm, $a = 1\,\mu$m, $d = 2\,\mu$m; ■: $h = 107 \pm 1$ nm, $a = 500$ nm, $d = 2\,\mu$m, ▲: $h = 90 \pm 2$ nm, $a = 500$ nm, $d = 1\,\mu$m. Data from the $a = 1\,\mu$m, $d = 2\,\mu$m nanopits were fit to the exponential function $v_{\text{pits}} \propto \exp(k v_{\text{slit}}^{-1})$ (green), while data from the $a = 500$ nm, $d = 2\,\mu$m nanopits were fit to a line (blue). Data from the $a = 500$ nm, $d = 1\,\mu$m nanopits were not well described over the full range by either an exponential or a linear function.

transport that builds on the work of Reisner *et al* by including the effects of a pressure-driven fluid flow on the equilibrium partitioning of DNA, and then calculating the free energy landscape that governs transport. Our goal is to build a model that captures the important qualitative features of our experiments in an intuitive manner, and with a minimal set of ingredients. We have consequently made significant simplifications, and ignored certain effects entirely that may be important in other regimes of device dimensions, DNA length, flow rate, quality of the solvent, etc. The implications of these assumptions will be discussed.

4.1. The free energy of nanoconfined DNA in an applied fluid flow

The theoretical model we consider is illustrated in figure 7, where the relevant parameters are also defined. A molecule is partitioned between the slit and N adjacent pits in a linear array. The length of DNA in the ith pit is denoted $L_{\text{p},i}$. The contiguity of the DNA molecule requires that there be $N - 1$ linker segments of DNA in the slit region, stretched between the occupied pits. The contour length in the ith linker is denoted $L_{\text{s},i}$. We also consider the leading segment of the DNA, which may venture downstream in the slit region a distance l_{s} past the last occupied pit.

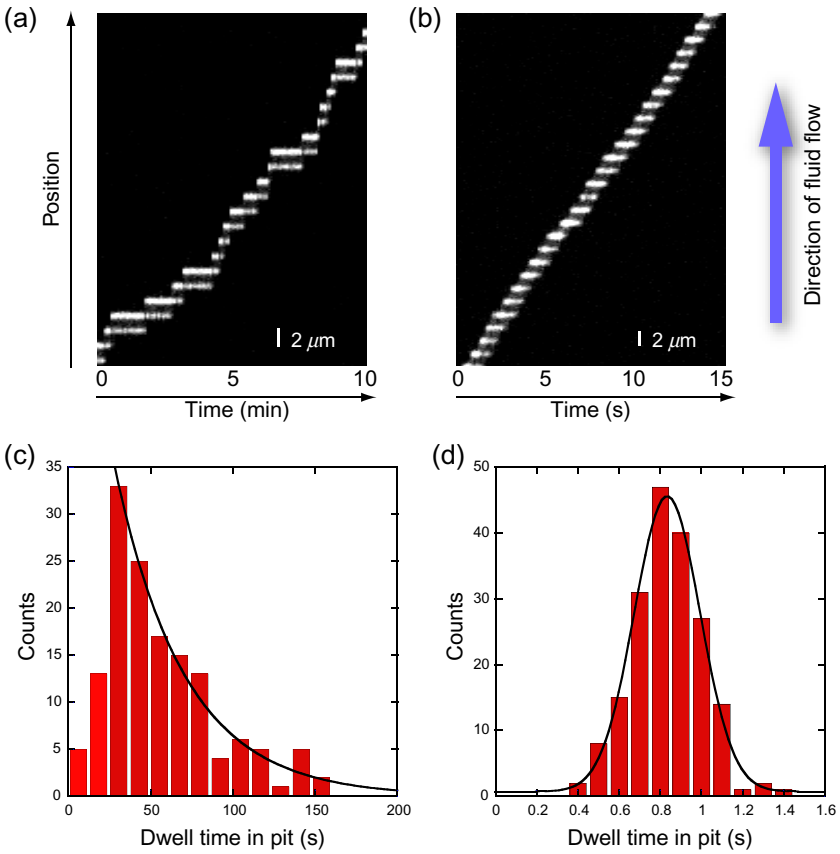

Figure 6. Video reslices of fluorescent λ-DNA moving across a linear array (vertical) of 500×500 nm pits spaced 1 μm apart in a 90 ± 2 nm deep slit. The positions and configurations of molecules along the nanopit array can be followed as a function of time. (a) The motion of three molecules under an applied pressure of 5 mbar ($v_{\text{slit}} = 1.21\ \mu\text{m s}^{-1}$). The average velocity across the pits was $v_{\text{pits}} = 0.050\ \mu\text{m s}^{-1}$. The different widths of the bright horizontal lines indicate the variance in DNA residence times in the pits. (b) The motion of a single molecule under an applied pressure of 40 mbar ($v_{\text{slit}} = 11.2\ \mu\text{m s}^{-1}$). The average velocity across the pits was $v_{\text{pits}} = 3.52\ \mu\text{m s}^{-1}$. The residence times of DNA in the pits were uniform. (c) A histogram of the DNA residence times in each pit for $v_{\text{slit}} = 1.21\ \mu\text{m s}^{-1}$. The solid line is an exponential fit to the data beyond the peak in the distribution. The decay time was 42 s. (d) A histogram of DNA residence times for $v_{\text{slit}} = 11.2\ \mu\text{m s}^{-1}$. The solid line is a Gaussian fit to the data. The width of the distribution was $\sigma = 0.23$ s.

This picture of DNA transport neglects configurations in which adjacent pits are joined by two or more linkers. It also ignores the possibility that herniated DNA 'hairpins' may escape the leading pit first, rather than the linear ends. In practice, we have never clearly observed multiple linkers between pits in equilibrium, which should be optically observable as two distinct strands, or a single linker with twice the normal fluorescence intensity. Furthermore, recent theoretical work by Wong and Muthukumar shows that hairpin escape only dominates over linear transport for high driving fields, and for sufficiently long molecules [19]. Our experiments, by contrast,

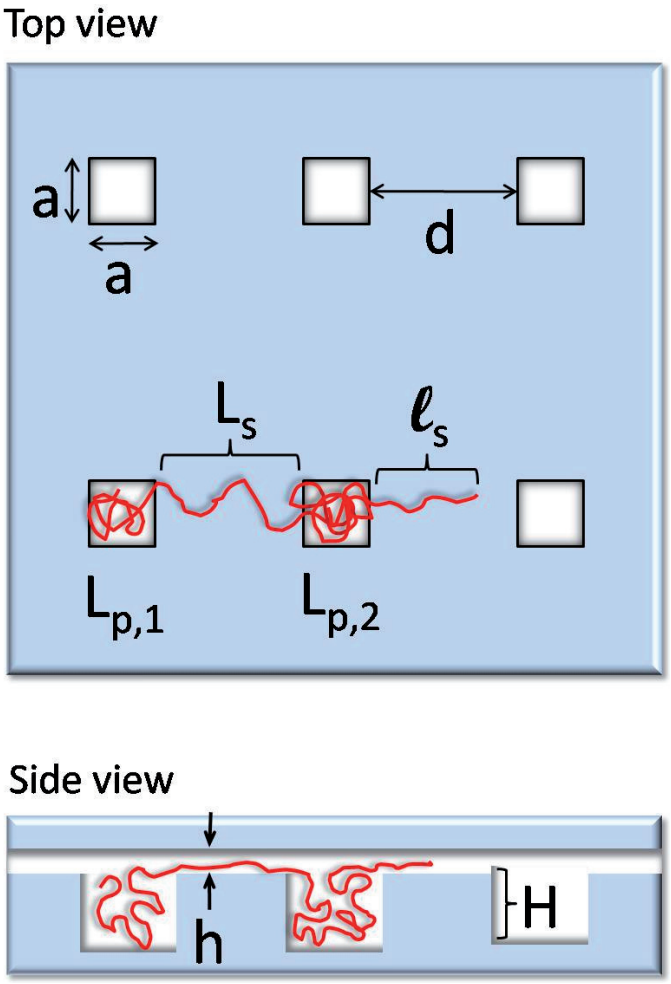

Figure 7. Schematic top-down and side views of DNA transport in nanopit arrays. The relevant device dimensions are the pit width a, the pit spacing d, the pit depth H and the slit depth h. The lengths of DNA contour partitioned in the various regions are indicated. The parameters illustrated here are relevant to the theoretical model described in the text.

measure DNA transport not far from equilibrium, and the nanopits restrict the length of DNA available to generate a hairpin.

Here we calculate the total free energy of a DNA molecule by summing contributions from the pits, the slit and the applied viscous forces, each considered separately.

The confinement free energy of the DNA in the slit region, F_s, is given by:

$$\frac{F_s}{k_B T} = A_s l_s + A_s \sum_{i=1}^{N-1} L_{s,i}, \tag{1}$$

where A_s is the confinement free energy per unit length in the slit and $k_B T$ is the thermal energy. F_s corresponds to the entropy loss of an ideal chain confined to the slit, and must be proportional to the confined DNA length as a consequence of the extensivity of the free energy. This property is predicted by all available polymer theories. A_s is expected to depend

nontrivially on parameters such as the slit height, the salt concentration and the polymer persistence length (P). Several expressions for A_s have been derived to describe different regimes of these parameters [20]–[24], but we note that these were all held constant in each nanofluidic device used in our experiments. We estimate $A_s \approx 6\,\mu\text{m}^{-1}$ for a $h = 100\,\text{nm}$ slit from $\Delta F \approx LP(x_1^{-2} + x_2^{-2} + x_3^{-2})$, a scaling expression for the free energy required to confine an ideal chain in a rectangular box with dimensions x_1, x_2 and x_3 [25]. This expression, which omits a numerical factor of order unity, has the advantage of providing sensible estimates for the confinement free energy in both slit and pit geometries.

The confinement free energy of DNA in the pits, F_p, is given by:

$$\frac{F_p}{k_B T} = \sum_{i=1}^{N} (A_p L_{p,i} + B L_{p,i}^2). \tag{2}$$

A_p is the entropic free energy per unit length of an ideal chain in a pit. We estimate $A_p \approx 1.6\,\mu\text{m}^{-1}$ for the $1\,\mu\text{m} \times 1\,\mu\text{m}$ pits and $A_p \approx 2.0\,\mu\text{m}^{-1}$ for the $500\,\text{nm} \times 500\,\text{nm}$ pits, using the same expression for the free energy as we used to estimate A_s. The second term in equation (2) accounts for the free energy of excluded volume interactions between DNA segments in the same pit. As two segments of DNA approach one another, their finite width leads to an increase in the free energy. The number of pairwise interactions between segments in the restricted volume of a pit scales as $L_{p,i}^2$. B is the coefficient for the self-exclusion interaction free energy. It has been argued that $B \sim w/V_{pit}$ in nanopit arrays, where V_{pit} is the pit volume and w is an effective chain thickness that can account for ionic-strength-dependent electrostatic interactions that enhance the DNA self-avoidance [14]. Assuming that $w \approx 10\,\text{nm}$, as previous equilibrium studies suggest [14], we estimate $B \approx 0.2$ and $0.05\,\mu\text{m}^{-2}$ for our 500 and 1000 nm wide pits, respectively.

Assuming linear and quadratic contributions to the free energy in equation (2) is analogous to considering the first two terms of a virial expansion for the polymer, which is appropriate in the regime where the excluded volume effect is intermediately strong. We have strong evidence that this was the case in our experiments because an entire DNA molecule could not fit within pits that were sufficiently small. Long DNA molecules were observed to spill out of small pits. The linear term alone cannot account for this, because if $B = 0$ the free energy is minimized by placing an entire molecule in a single pit, regardless of the contour length or the pit size. We ignored contributions to the free energy that were higher than second order because they were not needed to capture the essential physics. Furthermore, we estimate that even when confined to a single $1\,\mu\text{m}$ pit, λ-DNA occupied a volume fraction of only $\sim 1\%$, making third-order terms relatively unimportant.

When a DNA molecule occupies multiple pits, the linkers that must form between them are extended relative to their equilibrium conformations. This stretching of the linkers increases the free energy of the configuration. A simple way to account for this elasticity is to assume that each linker is an entropic spring, whose free energy is given by [20]:

$$\frac{F_{spring}}{k_B T} = \frac{3d^2}{4PL_{s,i}} \equiv \frac{C}{L_{s,i}}, \tag{3}$$

where P is the persistence length of DNA. Equation (3) is a reasonable approximation to the elastic response of DNA as long as the relative linker extension is below 50%.

The partitioning of DNA between the pits and the slit is constrained by the fixed DNA contour length:

$$L = l_s + \sum_{i=1}^{N} L_{p,i} + \sum_{i=1}^{N-1} L_{s,i}. \tag{4}$$

The confinement and spring components of the free energy, combined with the constant length constraint (equations (1)–(4)), can be used to predict the equilibrium configurations of DNA, as was previously reported [14]. Self-organization in the nanopit array was shown to occur because $A_p < A_s$, i.e. the nanopits are locally less confined than the nanoslit. In order to describe the transport of DNA, we will account for the influence of the driving force on the free energy.

The applied pressure-driven fluid flow exerts a viscous force on DNA. The force per unit contour length is proportional to the local speed of the fluid relative to the DNA. Modeling this interaction accurately is complex. In order to determine the fluid flow, it is necessary to consider the irregular geometry of the nanopit device, as well as disruptions of the flow caused by hydrodynamic radius of the DNA itself. However, the narrow slit regions are expected to dominate the free energy landscape, hence transport, because the fluid speed is faster there by a factor $\approx (h+H)/h$, and because the pits account for a relatively small fraction of the length occupied or traveled by the molecules ($a/(a+d) \leqslant 1/3$).

We simplify our model considerably by assuming a constant viscous force per unit length of DNA in the slit region, $k_B T f = v\xi_0$, where v is the average buffer velocity and ξ_o a friction factor per unit length. Under this definition, f has dimensions of inverse length squared, and the quantity fd^2 is a measure of energy, rescaled with respect to the thermal energy. Brochard and de Gennes [26] showed that since hydrodynamic interactions are screened in confined geometries, the hydrodynamic friction factor is indeed proportional to the contour length of the molecule.

Our approximation of the viscous driving force implicitly assumes that $v_{DNA} \ll v$ and, importantly, that the force on the DNA in the pits is zero. While these simplifications have made our transport model analytically tractable, and capture the qualitative features of our data, a more detailed description of the hydrodynamics is required to obtain accurate predictions. We note that within our model, applying pressure-driven flow is equivalent to driving the DNA across the pits by electrophoresis in a constant electric field, since DNA has a uniform zeta potential. For this reason, the pressure-driven transport of DNA between single pits is highly analogous to the entropic trapping phenomenon discovered and described by Han and Craighead [8, 16].

We take DNA transport to be a quasi-equilibrium situation, where the decrease in free energy of a downstream DNA segment is equal to the reversible work that must be done against the viscous force to bring the segment to a reference position, taken here to be the first (most upstream) pit. Accordingly, filling the ith pit with contour lowers the free energy by $fd(i-1)L_{p,i}$. Assuming that the contour in the ith linker is distributed uniformly in the space between the adjacent pits, the viscous force lowers its free energy by $fd(i-\frac{1}{2})L_{s,i}$. In addition, the leading segment of the DNA lowers the free energy by $\frac{1}{2}fl_s^2 - fd(N-1)l_s$. The overall viscous free energy, F_v, can be written:

$$-\frac{F_v}{k_B T} = fd\sum_{i=1}^{N}(i-1)L_{p,i} + fd\sum_{i=1}^{N-1}\left(i-\frac{1}{2}\right)L_{s,i} + fd(N-1)l_s + \frac{1}{2}fl_s^2. \tag{5}$$

The confinement free energy (equations (1) and (2)), the linker spring energy (equation (3)) and the viscous contribution (equation (5)) can all be combined to give the total free energy of a molecule occupying N pits in a pressure-driven flow:

$$\frac{\Delta F_N}{k_B T} = A_s l_s - \frac{1}{2} f l_s^2 - f d(N-1) l_s + \sum_{i=1}^{N} (A_p L_{p,i} + B L_{p,i}^2 - f d(i-1) L_{p,i}) + \sum_{i=1}^{N-1} \left(A_s L_{s,i} - f d \left(i - \frac{1}{2} \right) L_{s,i} + \frac{C}{L_{s,i}} \right). \tag{6}$$

4.2. The free energy landscape and DNA dynamics

It is useful to consider the free energy of a molecule as a function of the length of the leading segment, l_s, which plays the role of a reaction coordinate in our analysis. Since our transport model is based on quasi-equilibrium DNA configurations, for a given l_s, we minimize the free energy (equation (6)) in accordance with the constraint imposed by the fixed length of the DNA (equation (4)).

The shape of the resulting free energy landscape determines how DNA travels between the pits, and can explain the qualitatively different transport behavior observed in figures 5 and 6. In cases where an energetic barrier ΔF^* is present, thermal activation is required for the molecule to proceed. Assuming that such a barrier crossing process is rate limiting, the velocity of DNA along the linear nanopit array will be described by Kramers-type kinetics [27, 28]:

$$v_{pits} \propto \exp\left(-\frac{\Delta F^*}{k_B T} \right). \tag{7}$$

We note that for thermally activated transport, v_{pits} only obeys equation (7) *on average*. The motion is in fact stochastic in this regime, and we expect an exponential distribution of waiting times in each nanopit. It is also important to point out that our model assumes a fixed energy barrier, equal in magnitude to its value when the free energy of the DNA is minimized. In reality, we expect the height of the energy barrier to fluctuate as thermal motion dynamically affects the DNA conformations and its partitioning between the pits and the slit.

In the absence of an energy barrier, or if $\Delta F^* \ll k_B T$, then transport should be governed by the rate at which DNA contour is transferred from pit to pit. This process, which we call 'unspooling', is expected to lead to linear dynamics, i.e. $v_{pits} \propto v_{slit}$, but with a slower migration velocity than v_{slit}. The reason is that the nanotopography tends to direct the motion of DNA, threading contour through each pit, rather than allowing the entire molecule to travel forward at a uniform speed. This notion can be easily quantified within our simplified model. Consider the leading end of the propagating molecule, which will take a time $\tau = d/v_{slit}$ to reach the next downstream pit. Once the leading end reaches the pit, however, it will be delayed by an extra $\tau_{unspool} = (L_p - d)/v_{slit}$ as the upstream pit is emptied. The result will be a net velocity given by

$$v_{pits} = \frac{d}{\tau + \tau_{unspool}} = v_{slit} \frac{d}{L_p}. \tag{8}$$

The fact that our simplified model entirely neglects fluid flow in the pits almost certainly leads to an overestimate of $\tau_{unspool}$, especially for high fluid flow rates. Nevertheless, we expect that in the

unspooling regime, the motion of DNA is deterministic, with each step identical to the previous. For cases where $\Delta F^* \sim k_B T$, the timescales for thermal activation and unspooling dynamics may be comparable, and the motion can be a complex combination of the two mechanisms.

4.3. Single-pit occupancy

The free energy landscape of a DNA molecule partitioned between the nanoslit and a single pit ($N = 1$) is a useful place to begin. In this case, equation (6) reduces to

$$\frac{\Delta F_{N=1}}{k_B T} = A_p L_p + B L_p^2 + A_s l_s - \frac{1}{2} f l_s^2. \tag{9}$$

In the absence of fluid flow (i.e. $f = 0$), minimizing the free energy defined by equation (9) subject to the constant length constraint (4) gives the equilibrium contour length in the pit:

$$L_{p,1} = (A_s - A_p)/2B \equiv L_0. \tag{10}$$

Equation (10) defines an important length scale, L_0, corresponding to the maximum amount of DNA contour that a single pit can hold. If L_0 exceeds the available contour length, i.e. if $L_0 > L$, then the entire molecule will fall into the pit, and be held there by entropic forces. On the other hand, if $L > L_0$, then only an amount L_0 of contour will fill the pit, with the remainder in the slit, regardless of the length of the molecule. From our estimates of A_s, A_p and B, we predict that $L_0 \approx 44\,\mu$m for the $1\,\mu$m wide pits and $L_0 \approx 10\,\mu$m for the 500 nm wide pits. Since the contour length of stained λ-DNA lies between these two values, the predictions are consistent with our observation that a single molecules could fit entirely within a wide pit, but not a narrow one.

In general, a molecule can be found in states of varying pit occupancy (i.e. configurations with one pit, two pits, three pits occupied, etc), where states of occupancy N will have a corresponding occupancy probability $P(N)$, which depends on the geometry of the device and the length of the DNA molecule. Reisner *et al* [14] describe experiments and theory that address this issue. In the present study, we only observed single-pit occupancy states in 1000 nm wide pits for the timescales and ensemble size of our experiments, even though the probability of higher occupancy conformations may not be identically zero.

We now introduce fluid flow by allowing a finite value of f. Rewriting equation (9) as a function of l_s, and ignoring constant terms that do not affect the dynamics, gives the free energy landscape when the chain end is in the vicinity of the pit:

$$\frac{\Delta F_{N=1}(l_s)}{k_B T} = 2B(L_0 - L)l_s + \left(B - \frac{1}{2} f\right) l_s^2. \tag{11}$$

Let us first consider the case $L < L_0$, where the entire molecule can fit inside a single pit, illustrated in figure 8, and closely resembling the situation that was observed for λ-DNA in $1 \times 1\,\mu$m pits (see figure 1(c)). Equation (11) reveals two regimes that are relevant to single-pit transport. In the low-force regime ($f \leqslant B$), the free energy increases monotonically with l_s. Excluded volume interactions in the pit define the limits of this regime, so it is informative to consider their role. As the molecule is extracted from the pit, the decrease in excluded volume interactions generates a retraction force that grows linearly with l_s. (In previous models of

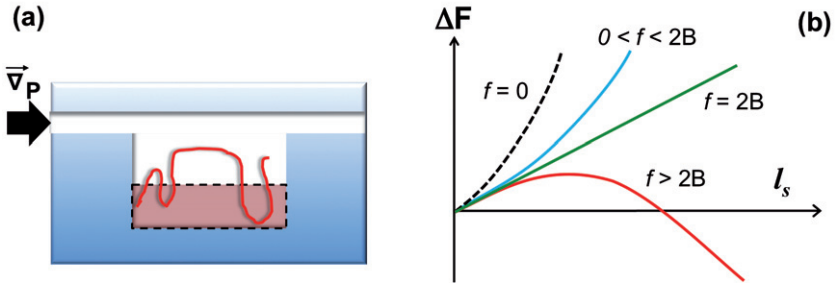

Figure 8. (a) An illustration of DNA occupying a single pit. The total DNA contour length is below the capacity of the pit ($L < L_0$), indicated by the pit-filling fraction shaded red. (b) A schematic of the corresponding free energy landscape for low (blue), critical (green) and high (red) applied pressures, and at equilibrium ($f = 0$, dashed). The energy barrier appears at pressures beyond the critical value. The barrier can be lowered, but not eliminated, by the application of high driving forces.

entropic trapping, by contrast, self-interactions are ignored, resulting in a constant retraction force.) The retraction force counters the driving force, which also grows linearly with l_s. As long as $f < 2B$, the retraction force exceeds the driving force and the molecule remains strongly trapped within the pit. In this low-force regime, DNA transport requires thermal fluctuations large enough to extend the leading end of the molecule all the way to the next pit. The high free energy barrier associated with such an event strongly suppresses transport.

High applied forces ($f > 2B$) can exceed the self-exclusion force, and compete with forces originating from the confinement entropy. In this high-force regime, the free energy develops a maximum at $l_s = 2B(L_0 - L)/(f - 2B)$, where the height of the free energy barrier is given by $\Delta F^*/k_BT = 2B^2(L_0 - L)^2/(f - 2B)$. Clearly, increasing the pressure-driven fluid flow lowers the activation barrier and shifts its location closer to the occupied pit. The existence of a free energy barrier means that transport between pits must be thermally activated. Sufficiently large viscous forces therefore promote transport on experimental timescales by reducing the barrier height to $\approx k_BT$. For large applied viscous forces ($f \gg 2B$), the migration velocity is given by

$$v_{\text{pits}} = v_0 \exp\left(-\frac{\Delta F^*}{k_BT}\right) \approx v_0 \exp\left(-\frac{2B^2(L_0 - L)^2 f^{-1}}{k_BT}\right). \tag{12}$$

According to equation (12), the applied fluid flow can speed up the thermally activated transport by lowering the activation barrier, but the barrier cannot be completely eliminated.

It is also possible, if $L > L_0$, for a molecule to completely fill a single pit, and then spill over into the nanoslit without occupying a second pit, as illustrated in figure 9. The molecule remains trapped by the pit due to the excluded volume forces described above. It can be shown that in the limit of weak applied forces ($f < 2B$), it is possible to pull contour out of the pit, and to reach a stable configuration at some finite extension of the leading segment, l_s. The energy barrier that must be overcome for transport in this case corresponds to the leading end of the molecule reaching the next pit in an array, or the trailing end of the molecule completely leaving

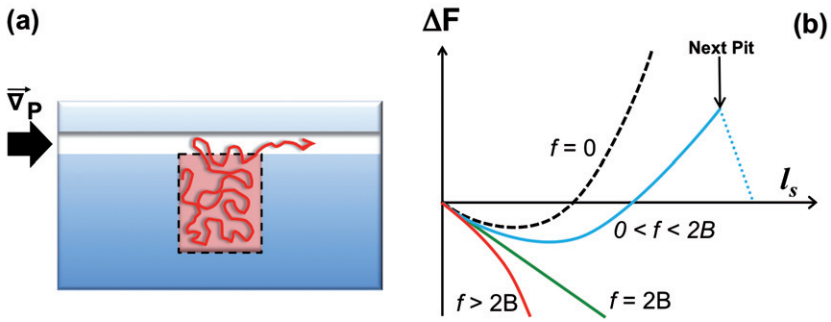

Figure 9. (a) An illustration of DNA filling a single pit, and spilling over into the nanoslit. The pit fills to capacity, indicated by the pit-filling fraction shaded red, and contour enters the nanoslit when $L > L_0$. (b) A schematic of the corresponding free energy landscape for low (blue), critical (green) and high (red) applied pressures, and at equilibrium ($f = 0$, dashed). The energy barrier is completely eliminated beyond the critical driving force $f_c = 2B$.

the pit. An applied force exceeding the critical value, $f_c = 2B$, overcomes the restoring force. The energy barrier disappears, and the molecule is pulled out of the pit.

4.4. Two-pit occupancy

A molecule that occupies multiple pits at equilibrium is qualitatively different from a single-pit molecule because the former is able to shift contour between the pits and the linkers to minimize its free energy. This distinction results in strikingly different transport dynamics than in the case where a molecule fits entirely into a single pit. Here, we describe the details of a two-pit molecule, i.e. $N = 2$. The qualitative features of two-pit DNA transport, illustrated in figure 10, are shared by higher N situations.

From equation (6), the free energy of DNA partitioned between two pits, a linker, and a leading segment in the nanoslit can be written as

$$\frac{\Delta F_{N=2}}{k_B T} = A_p(L_{p,1} + L_{p,2}) + B(L_{p,1}^2 + L_{p,2}^2) + A_s(L_s + l_s) + \frac{C}{L_s} - \frac{1}{2} f d L_s - f d L_{p,2} - f d l_s - \frac{1}{2} f l_s^2. \tag{13}$$

At equilibrium, it had been possible to assume that the occupancy of each of the N pits was the same. The fluid flow breaks the symmetry between the pits. We therefore need to minimize the free energy described by equation (13) for arbitrary $L_{p,i}$ and L_s, subject to fixed contour length condition and fixed l_s. The method of Lagrange multipliers can be used to give the following system of equations:

$$0 = \frac{\partial \Delta F_N}{\partial L_{i,j}} - \lambda \frac{\partial L}{\partial L_{i,j}}, \tag{14}$$

where λ is the Lagrange parameter, and the subscripts $i = s, p$ and $j = 1, 2$ indicate that a separate equation is obtained for the DNA contour in each pit and the slit.

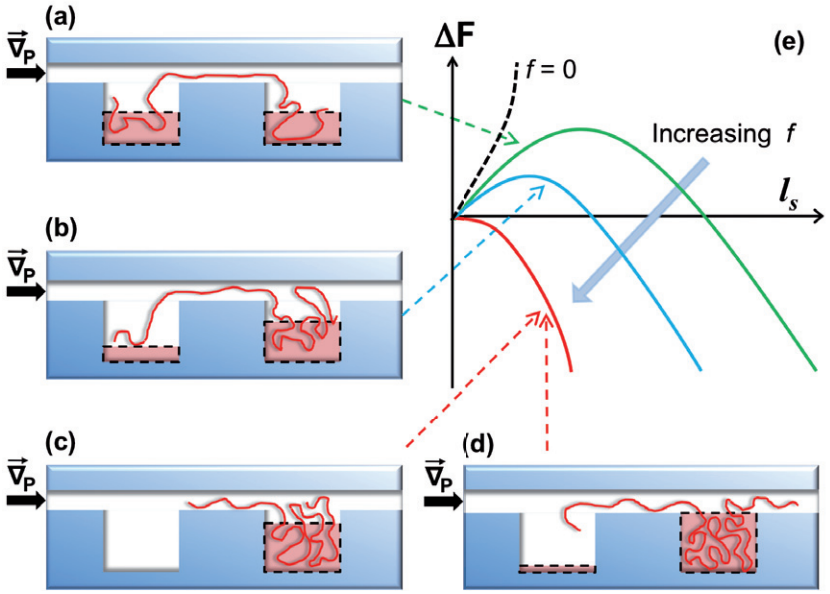

Figure 10. Illustrations of DNA transport for a two-pit configuration. The pit-filling fractions are shaded red, and the situation is sketched for increasing applied pressures. (a) At equilibrium ($f = 0$), both pits contain equal amounts of DNA contour. (b) For low forces ($f < f_{c,1}$, $f_{c,2}$), DNA contour is transferred from the upstream pit to the downstream pit, but both pits remain partially filled. Beyond a critical force, either (c) the trailing pit is emptied ($f > f_{c,1}$), or (d) the leading pit reaches its capacity ($f > f_{c,2}$). (e) The free energy landscape corresponding to each situation is sketched. At equilibrium ($f = 0$, dashed), the free energy increases monotonically. The energy barrier that appears at small applied pressures (green) is lowered by increasing forces (blue), and completely eliminated beyond either the critical pit-emptying or pit-filling driving force (red).

To minimize its free energy, the DNA molecule partitions its contour between the two pits as follows:

$$L_{p,1} = L_0 - \frac{C}{2BL_s^2} - \frac{fd}{4B}, \tag{15}$$

$$L_{p,2} = L_0 - \frac{C}{2BL_s^2} + \frac{fd}{4B}. \tag{16}$$

In order to solve for L_s, we could insert equations (15) and (16) into the contour length constraint (equation (4)), which leads to a cubic equation. However, the basic physics that is important for understanding DNA transport in the two-pit configuration is already contained in the expressions for $L_{p,1}$ and $L_{p,2}$ above.

We first consider the role of entropic elasticity. In the absence of this term ($C = 0$), the equilibrium DNA configuration would fill each pit to capacity with L_0 of contour, with the remainder of the molecule forming the linker (assuming it is longer than d). This configuration

is unstable, because there is no energetic cost to transferring DNA contour from the linker, through the leading pit, and towards the next pit (extending l_s), i.e. there is no energy barrier. A finite entropic elasticity of the linker acts to stabilize the equilibrium configuration. The second terms in equations (15) and (16) show that the linker pulls contour out of each pit, lowering the occupancy of each by an amount $C/2BL_s^2$ relative to the maximum value L_0. In this case, extending the leading end of the molecule towards the next pit costs both confinement free energy and entropic spring energy, i.e. there is an energy barrier, and transport must be thermally activated.

The effect of the viscous driving force is to lower, and ultimately eliminate, the energy barrier. The third terms in equations (15) and (16) show that an amount $fd/4B$ of contour is transferred from the upstream pit to the downstream pit when a pressure is applied. This lowers the energetic cost of drawing contour from the leading pit to extend l_s, thereby lowering the energy barrier. Furthermore, the transfer of contour between the pits cannot be carried out for arbitrarily high f. Beyond $f_{c,1} = 4BL_0/d - 2C/L_s^2$, the upstream pit will be completely empty ($L_{p,1} = 0$), and beyond $f_{c,2} = 2C/L_s^2$, the downstream pit will have reached its maximum capacity ($L_{p,2} = L_0$). In both cases, the free energy barrier disappears: once the upstream pit empties, there is no energetic penalty for shifting the linker into the leading pit until it reaches its capacity, and then transferring the remaining linker contour downstream towards the next pit (this in fact lowers the free energy). The filling of the downstream pit, on the other hand, means that the viscous force there exceeds the entropic elastic force of the linker. In this situation, the free energy is again lowered by transferring contour from the linker, through the leading pit and extending l_s. We consequently expect a transition from stochastic, thermally activated transport to the deterministic unspooling regime beyond the critical pit-emptying or pit-filling force, whichever is lower.

Finally, we note that since the amount of contour transferred between the pits is proportional to d, decreasing the spacing between pits, while holding the pit dimensions constant, will tend to stabilize the configuration and lead to a higher critical driving force. We also point out that the most stable two-pit configuration, for which the critical force is highest, corresponds to the situation where each pit is filled halfway to capacity, i.e. $L_{p,1} = L_{p,2} = L_0/2$.

4.5. Arbitrary multiple-pit occupancy

It is possible to make some general statements about the physics of a DNA molecule occupying an arbitrary number of pits, starting from the general expression for the free energy, equation (6). Carrying out the minimization procedure of equation (14) for a segment in an arbitrary pit, $L_{p,i}$, and an arbitrary linker segment, $L_{s,j}$, gives the following relationship between them at equilibrium:

$$L_{p,i} = L_0 - \frac{C}{2BL_{s,j}^2} + \frac{fd}{4B}(2i - 2j - 1). \tag{17}$$

Since $L_{p,i}$ cannot depend on the choice of j, $C/2BL_{s,j}^2 - jfd/2B = K$ must be independent of j. We choose $K = \delta + Nfd/4B$, where δ is a length that can depend on f, and find that the occupancy of the ith pit at equilibrium can be written in the following form:

$$L_{p,i} = L_0 - \delta + \frac{fd}{4B}(2i - (N+1)). \tag{18}$$

The general expression for $L_{p,i}$ above shows that the partitioning of DNA between the slit and an arbitrary number of pits ($N > 1$) is similar to the two-pit case (equations (15) and (16)), to which equation (18) reduces for $N = 2$. Accordingly, we interpret δ as a length of contour removed from the otherwise filled pits by entropic spring forces, which stabilizes the configuration and gives rise to an energy barrier. Viscous forces transfer contour from upstream pits to downstream pits, with the greatest length of contour removed from the trailing pit, and with the greatest length transferred to the leading pit. As in the two-pit case, the energy barrier disappears when the force is sufficient to either fill the leading pit to capacity, or to completely empty the trailing pit. We therefore predict a transition from thermally activated transport to a linear, unspooling transport regime beyond a critical force for all multiple-pit configurations (although the critical force may be very small).

5. Discussion

We can draw some basic conclusions from the above analysis. Single-pit states for which the entire molecule fits in the pit ($L < L_0$) are the most stable. The DNA transport dynamics in this situation should be in the thermally activated regime for all values of the applied flow. Increasing the number of occupied pits destabilizes the configuration, as the molecule can now transfer contour between the upstream and downstream pits via the nanoslit. The dynamics of DNA transport in multiple-pit states can exhibit both thermally activated behavior and linear, unspooling behavior, with a crossover force that depends on the details of the device geometry.

Our experiments were in excellent qualitative agreement with this picture. For the single-pit occupancy, $1 \times 1\,\mu$m pits, the observed dynamics were well described by equation (12). Figure 11 replots the v_{pits} data from figure 5 on semilog axes as a function of v_{slit}^{-1}. The 1×1 μm pit data lie on a straight line. This $\log(v_{pits}) \propto -1/v_{slit}$ dependence over the full range of applied pressures was predicted by the transport model. It is interesting to note that the activated transport picture describes the experimental data well even at high applied pressures, where v_{pits} approaches v_{slit}. The unspooling picture of equation (8), on the other hand, predicts that v_{pits} should saturate at a significantly lower velocity. The discrepancy is likely the result of our simplified model of the viscous force, which completely ignores the effects of fluid flow in the pits.

For the 500×500 nm pits spaced $1\,\mu$m apart, which gave multiple-pit configurations at equilibrium ($N = 2$), we found that the dynamics were in the thermally activated transport regime for low applied pressures, but then transitioned to the unspooling regime at a critical value of $v_{slit} \sim 4\,\mu\text{m s}^{-1}$ (see figure 5). Strong evidence of this transition can be found in the detailed DNA dynamics presented in figure 6: the motion of the molecule was stochastic at low v_{slit}, but deterministic at higher v_{slit}. Thus, we confirm experimentally a fundamental prediction of the theoretical analysis: the dynamics of multi-pit configurations crossover from thermally activated to unspooling dynamics at a critical applied flow.

Since the height of the energy barrier is expected to depend nonlinearly on f^{-1} in the multi-pit, thermally activated regime, it is not possible to plot a straight line through the data to quantify the energy barrier, even for high v_{slit}^{-1}. The relatively high value of v_{pits} in the high v_{slit}^{-1} limit was nevertheless surprising. We speculate that fluctuations of the energy barrier induced by thermally fluctuating occupancy of the pits may be relevant in this regime.

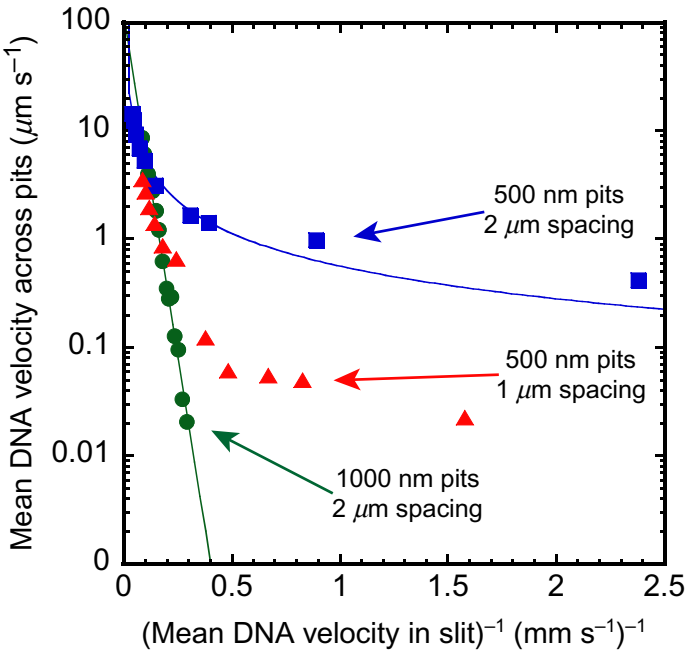

Figure 11. A semilog plot of v_{slit} versus v_{slit}^{-1} for the three device geometries tested (same data as in figure 5). The $1 \times 1\ \mu$m pit data were fit to the thermally activated velocity predicted by equation (12) for single-pit occupancy (green line). Data from the 500×500 nm pit, $2\ \mu$m spacing devices were fit to a linear function predicted by equation (8) for unspooling dynamics.

For the 500×500 nm pits spaced $2\ \mu$m apart, we found that the DNA dynamics were in the unspooling regime for all values of the applied flow: v_{pits} was linearly proportional to v_{slit}, though reduced in magnitude, as seen by the fits in figures 5 and 11. It is possible that the crossover velocity between unspooling and thermally activated dynamics in the 500×500 nm pits with $2\ \mu$m spacings was too small for us to observe. We expect that a higher d will reduce the critical force, so it is unsurprising that the $d = 1\ \mu$m case would have a higher threshold than the $d = 2\ \mu$m case.

Finally, note that when we compare the two geometries with unspooling dynamics, the behavior of v_{pits} was roughly consistent with what equation (8) predicts. We predicted $v_{\text{pits}} \sim d$ and observed that by doubling the spacing between the 500×500 nm pits from $d = 1\ \mu$m to $d = 2\ \mu$m, the unspooling velocity increased by a factor that, despite varying with v_{slit}, was approximately two.

6. Conclusions

In conclusion, we have developed a picture of DNA transport across linear arrays of nanopits in which the dynamics depend crucially on the partitioning of DNA in the pits and on the magnitude of the driving force. The physics revealed here may be relevant to other nanofluidic structures or contexts, such as near surfaces with nanoscale roughness. Our results also suggest that by carefully designing the nanotopography of a nanofluidic device, it is possible to tailor its transport characteristics. Such control over the motion of single molecules could find use

in lab-on-a-chip technology. In the future, we hope to build a quantitative understanding of how the energy barriers depend on the details of device geometry, and to investigate the effect of varying DNA length on transport dynamics. Since half-filled pits at equilibrium are more stable configurations than filled pits, our transport model anticipates that DNA mobility can be a non-monotonic function of contour length. We also hope to explore the effects of temperature variation and possible hydrodynamic interactions between molecules along the arrays.

Acknowledgments

We acknowledge A Kristensen for access to the cleanroom facilities in which the nanopit arrays were fabricated, S C Ying for useful discussions regarding theoretical modeling of DNA transport, and support for this work from the National Science Foundation under grant number DMR-0805176 and from Brown University.

References

[1] Volkmuth W D and Austin R H 1992 DNA electrophoresis in microlithographic arrays *Nature* **358** 600–2
[2] Tegenfeldt J O, Prinz C, Cao H, Huang R L, Austin R H, Chou S Y, Cox E C and Sturm J C 2004 Micro- and nanofluidics for DNA analysis *Anal. Bioanal. Chem.* **378** 1678–92
[3] Li J, Stein D, McMullan C, Branton D, Aziz M J and Golovchenko J A 2001 Ion-beam sculpting at nanometre length scales *Nature* **412** 166–9
[4] Dekker C 2007 Solid-state nanopores *Nat. Nanotechnol.* **2** 209–15
[5] Baba M, Sano T, Iguchi N, Iida K, Sakamoto T and Kawaura H 2005 DNA size separation using artificially nanostructured matrix *Appl. Phys. Lett.* **5** 1468
[6] Fan R, Karnik R, Yue M, Li D, Majumdar A and Yang P 2003 DNA translocation in inorganic nanotubes *Nano Lett.* **83** 1633–7
[7] Stein D, van der Heyden F H J, Koopmans W J A and Dekker C 2006 Pressure-driven transport of confined DNA polymers in fluidic channels *Proc. Natl Acad. Sci. USA* **103** 15853–8
[8] Han J and Craighead H G 2000 Separation of long DNA molecules in a microfabricated entropic trap array *Science* **288** 1026–9
[9] Tegenfeldt J O *et al* 2004 The dynamics of genome-length DNA molecules in 100-nm channels *Proc. Natl Acad. Sci. USA* **101** 10979–83
[10] Reccius C H, Mannion J T, Cross J D and Craighead H G 2005 Compression and free expansion of single DNA molecules in nanochannels *Phys. Rev. Lett.* **95** 268101
[11] Riehn R, Lu M, Wang Y-M, Lim S F, Cox E C and Austin R H 2005 Restriction mapping in nanofluidic devices *Proc. Natl Acad. Sci. USA* **102** 10012–6
[12] Jo K, Dhingra D M, Odijk T, de Pablo J J, Graham M D, Runnheim R, Forrest D and Schwartz D C 2007 A single molecule barcoding system using nanoslits for DNA analysis *Proc. Natl Acad. Sci. USA* **104** 2673–8
[13] Reisner W, Morton K J, Riehn R, Wang Y M, Yu Z, Rosen M, Sturm J C, Chu S Y, Frey E and Austin R H 2005 Statics and dynamics of single DNA molecules confined in nanochannels *Phys. Rev. Lett.* **94** 196101
[14] Reisner W, Larsen N, Flyvbjerg H, Tegenfeldt J and Kristensen A 2009 Directed self-organization of single DNA molecules in a nanoslit via embedded nanopit arrays 2009 *Proc. Natl Acad. Sci. USA* **106** 79–84
[15] Smith D E, Perkins T T and Chu S 1996 Dynamic scaling of DNA diffusion coefficients *Macromolecules* **29** 1372–3
[16] Han J and Craighead H 2002 Characterization and optimization of an entropic trap for DNA separation *Anal. Chem.* **74** 394–401
[17] Ed Rai-Choudhury P 1997 *SPIE Handbook of Microlithography, Micromachining and Microfabrication* vol 1 (Bellingham, WA: SPIE Optical Engineering Press)

[18] Perkins T, Smith D and Chu S 1997 Single polymer stretching in an elongation flow *Science* **276** 2016–21
[19] Wong C T A and Muthukumar M 2008 Scaling theory of polymer translocation into conned regions *Biophys. J.* **95** 3619–27
[20] de Gennes P G 1979 *Scaling Concepts in Polymer Physics* (Ithaca, NY: Cornell University Press)
[21] Odijk T 1983 The statistics and dynamics of confined or entangled stiff polymers *Macromolecules* **16** 1340–4
[22] Brochard-Wyart F, Tanaka T, Borghi N and de Gennes P G 2005 Semiflexible polymers confined in soft tubes *Langmuir* **21** 4144–8
[23] Burkhardt T 1997 Free energy of a semiflexible polymer in a tube and statistics of a randomly-accelerated particle *J. Phys. A: Math. Gen.* **30** L167–72
[24] Sakaue T 2007 Semiflexible polymer confined in closed spaces *Macromolecules* **40** 5206–11
[25] Doi M and Edwards S F 1986 *The Theory of Polymer Dynamics* (New York: Oxford University Press)
[26] Brochard F and de Gennes P G 1977 Dynamics of confined polymer chains *J. Chem. Phys.* **67** 52–6
[27] Kramers H A 1940 Brownian motion in a field of force and the diffusion model of chemical reactions *Physica* **7** 284–304
[28] Hänggi P, Talkner P and Borkovec M 1990 Reaction-rate theory: fifty years after Kramers *Rev. Mod. Phys.* **62** 251–342